

Next-Best-Trajectory Planning of Robot Manipulators for Effective Observation and Exploration

Heiko Renz, Maximilian Krämer, Frank Hoffmann and Torsten Bertram

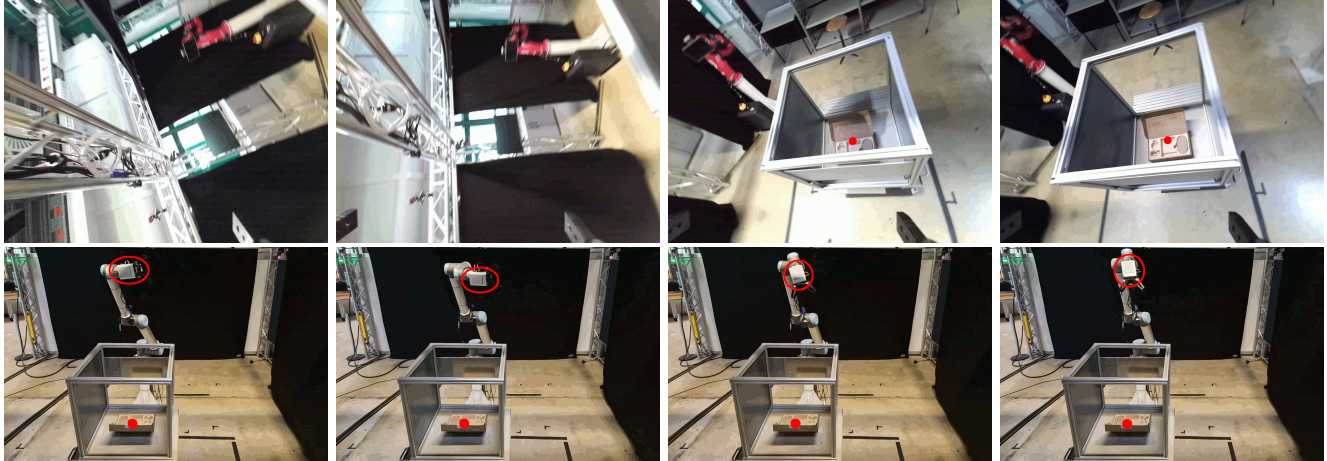


Fig. 1: The camera view (top row) and the robot (bottom row) without optimizing the Information Gain towards the Point of Interest (red dot) and during Next-Best-Trajectories with weights of $w_1 = 5$, $w_1 = 25$, and $w_1 = 50$ (left to right).

Abstract—Visual observation of objects is essential for many robotic applications, such as object reconstruction and manipulation, navigation, and scene understanding. Machine learning algorithms constitute the state-of-the-art in many fields but require vast data sets, which are costly and time-intensive to collect. Automated strategies for observation and exploration are crucial to enhance the efficiency of data gathering. Therefore, a novel strategy utilizing the Next-Best-Trajectory principle is developed for a robot manipulator operating in dynamic environments. Local trajectories are generated to maximize the information gained from observations along the path while avoiding collisions. We employ a voxel map for environment modeling and utilize raycasting from perspectives around a point of interest to estimate the information gain. A global ergodic trajectory planner provides an optional reference trajectory to the local planner, improving exploration and helping to avoid local minima. To enhance computational efficiency, raycasting for estimating the information gain in the environment is executed in parallel on the graphics processing unit. Benchmark results confirm the efficiency of the parallelization, while real-world experiments demonstrate the strategy’s effectiveness.

I. INTRODUCTION

Observing objects and exploring unknown environments are essential for robots to gather task-relevant information. Observation collects object data, while exploration navigates uncharted areas for new insights.

This work is funded by the Deutsche Forschungsgemeinschaft (DFG, German Research Foundation) - 497071854.

All authors are with the Institute of Control Theory and Systems Engineering, TU Dortmund University, Dortmund, Germany. [heiko.renz, maximilian.kraemer, frank.hoffmann, torsten.bertram]@tu-dortmund.de

This study presents a novel local trajectory planner that maximizes the Information Gain (IG) along its path using a Graphics Processing Unit (GPU)-accelerated online local Information Distribution (ID). By aggregating IGs from multiple perspectives, the ID offers to optimize the camera view during trajectory planning. A global ergodic trajectory planner [1] provides a reference trajectory, integrating exploration and observation while avoiding local minima.

The observation data, collected from various sensor modalities, models the environment with an online voxel map for the Next-Best-Trajectory (NBT) strategy. Unlike Next-Best-View (NBV) approaches, NBT maximizes the IG along the entire trajectory rather than focusing on a single perspective, offering a more comprehensive view. The voxel map estimates the IG from different perspectives, with unknown-state voxels holding the highest IG potential, while free or occupied voxels still provide useful environmental updates. A parallelized raycasting algorithm computes IGs within the environment. Fig. 1 illustrates the benefits of prioritizing the IG when observing a Point of Interest (PoI).

The key contributions of this work are summarized as follows, and the code is publicly available as a branch of the Moving Horizon Planner (MHP)¹ [2]:

- Online local ID using raycasting to estimate IGs from multiple perspectives in a voxelized environment, building an IG Point Cloud (PC) based on the voxel map;
- Parallelization of the IG algorithm on a GPU to improve computational efficiency;

¹<https://github.com/rst-tu-dortmund/mhp4hri/tree/next-best-trajectory-github>

- Integration of the ID into an MHP to determine the NBT for a robot manipulator;
- Extension of the MHP to track a global ergodic trajectory [1], enhancing exploration and preventing standstills.

II. RELATED WORK

This section explores mapping techniques for calculating IGs and robotic planning strategies integrating perspective information for goal selection.

Mapping Techniques: Mapping is fundamental in robotics for environmental representation and planning. The choice of technique – ranging from 2.5D height maps [3] to voxel maps [4], [5], [6] and direct PC analysis [7] – depends on specific needs and constraints.

GPU acceleration reduces the computational cost of 3D map generation from PCs [5]. Voxel maps, notably *OctoMap* [4], use an octree structure to improve memory efficiency and address height map limitations. *OctoMap-RT* [5] extends this by leveraging GPU for faster map generation. Other GPU-based voxel mapping methods include *G-VOM* [8], optimized for real-time off-road exploration, and *Voxblox++* [9], which integrates RGB-D data for instance-aware semantic mapping. *UfoMap* [6] improves *OctoMap* by explicitly marking free, occupied, and unknown areas, making it ideal for IG tasks. We use *UfoMap* for its ability to represent unknown space and its publicly available code, setting it apart from alternatives.

Reconstruction and Exploration: Many mapping and robotic exploration strategies survey or reconstruct environments and objects. Robots navigate different locales to acquire new insights, strategizing their motion toward the optimal perspective – the NBV – to enhance environmental knowledge [3], [10], [11], [12].

One approach to explore unknown areas employs drones with sampling-based planners [10]. Frontier-based strategies further improve exploration efficiency [11]. Research also extends to robotic manipulators, with voxel-based methods enabling autonomous scene navigation and analysis [12]. A raycasting algorithm evaluates potential IGs from randomized perspectives around the PoI to estimate the NBV. However, it fails to account for occlusions or misorientation as the robot moves. Increasing perspectives mitigates occlusions but requires constant replanning. The NBT strategy conversely optimizes the entire trajectory to maximize gain under given constraints instead of individual perspectives. Direct robot-environment interaction is crucial for capturing details in unknown environments [3], particularly for revealing hidden objects, though it is less effective for documenting changes.

Object reconstruction is another key task where NBVs provide guidance. Incorporating uncertainties and probabilities into IG calculations improves reconstruction quality [13]. Expanding the NBV approach to sequence perspectives further enhances reconstruction [14].

Next-Best-Trajectory: However, a limitation of these methods is their failure to account for the potential IGs that could arise between perspectives despite optimizing sequences for reconstruction. An NBT approach has been proposed for drone exploration to optimize the drone’s trajectory in

a tree-based manner, considering possible IGs in a voxel map [15]. The method also applies *UfoMap* due to modeling unknown space and embeds the IG into an exploration-rapidly-exploring-random tree and a nonlinear model predictive control framework to control the drone. Further work includes ergodic coverage and optimization techniques [1]. These methods allow exploration based on ergodicity, ensuring that the robot explores the environment uniformly and efficiently or based on a desired target distribution representing areas of different estimated IGs. These methods, however, are designed and tested on mobile robots or drones and not for robot manipulators in shared workspaces with humans or are not executable online. Nevertheless, an adapted version of [1] extends our local trajectory planner to follow a global ergodic trajectory, exploring the environment and avoiding freezing robot problems.

III. ONLINE LOCAL INFORMATION DISTRIBUTION

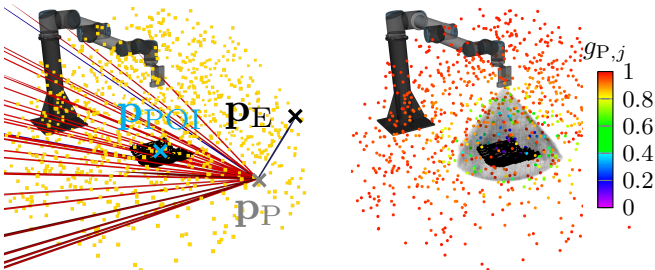
Our approach extends *UfoMap* [6] to estimate IGs from various perspectives around a PoI whenever a new PC is captured. New PCs are captured online during robot motion with an end-effector camera, accounting for new occlusions and environmental changes. These perspective-based IGs contribute to building a local ID, enabling the evaluation of IG for the NBT at different trajectory poses. The local ID is linked to entropy, which measures the uncertainty in voxel occupancy. High entropy signifies a high level of uncertainty, which corresponds to a high value in the ID. This is because perspectives that reduce environmental uncertainty result in a significant increase in IG.

The first step of generating the ID applies a voxel filter from the *Point Cloud Library* [16] to thin out the PC, thus boosting the voxel map creation. Generating the ID encompasses three main steps: selecting perspectives, calculating endpoints, and determining IG through raycasting.

Perspective Selection: To establish a local ID, different starting points for perspectives $\mathbf{p}_P = [p_{P,x} \ p_{P,y} \ p_{P,z}]^T \in \mathbb{R}^3$ are sampled around the chosen PoI $\mathbf{p}_{POI} = [p_{POI,x} \ p_{POI,y} \ p_{POI,z}]^T \in \mathbb{R}^3$. The PoI is modeled as a single point in the center of an object, simplifying the process of calculating the ID. A uniform distribution of N_P perspectives within a spherical area surrounding the PoI is adopted for thorough coverage. To ensure an even spread, observation points are generated on the sphere’s surface, done efficiently using Muller’s method [17]. The points initially generated on the unit sphere’s surface are scaled to match the desired sphere radius r_S around the PoI. To achieve a uniform distribution of points in this sphere, the surface points are scaled by a uniformly distributed value $X_R \sim \mathcal{G}(0, 1)$ as:

$$\mathbf{p}_P = r_S X_R^{1/3} \frac{X_k}{\sqrt{\sum_{l \in \{x,y,z\}} X_l^2}} \quad \text{for } k \in \{x, y, z\}, \quad (1)$$

with normal distributed values $X_{\{x,y,z\}} \sim \mathcal{N}(\mu = 0, \sigma = 1)$ in the Euclidean space x, y, z . Incorporating the $1/3$ power is required for achieving a uniform distribution of points within the sphere, accounting for the 3D sphere’s surface area



(a) Perspectives (yellow) including exemplary rays for a single perspective (red, corners in blue) with $s_G = 100$ (b) Local ID with $s_G = 50$. Color representing the IG for each perspective. The grey cone marks free voxels in front of objects in the camera FoV.

Fig. 2: Raycasting (a) and ID results (b) with $N_P = 1000$.

variation. For the radius r_S , a value of $r_S = 1$ m is chosen to ensure that the perspectives are close enough to the PoI to capture details. The orientation of each perspective is then determined by the vector originating from the perspective's starting point \mathbf{p}_P to the PoI \mathbf{p}_{POI}

Endpoint Calculation: Once the perspectives \mathbf{p}_P are determined, the process calculates for each \mathbf{p}_P N_E endpoints $\mathbf{p}_E = [p_{E,x} \ p_{E,y} \ p_{E,z}]^T \in \mathbb{R}^3$ inside the camera's Field of View (FoV). Each perspective's frustum center is oriented towards the PoI, and the camera's far frustum plane is at the camera's range d_{Cam} . The central point is adjusted along the x and y axes by d_h and d_v to calculate the peripheral points on the camera's far frustum plane. This adjustment considers the camera's vertical and horizontal FoV (FoV_v and FoV_h) and its range d_{Cam} using the formulas $d_h = d_{Cam} \cdot \tan(FoV_h/2)$ and $d_v = d_{Cam} \cdot \tan(FoV_v/2)$. The calculated points delineate the four border rays of the frustum and serve as limitations for the endpoint rays. Evaluating IGs from only the frustum endpoints is insufficient since, depending on the camera's parameters d_{Cam} , FoV_v and FoV_h , these border rays exhibit distances that can be greater than objects to model. Hence, N_E endpoints \mathbf{p}_E are sampled within the frustum's borders on a grid. The distance between these endpoints is determined by the voxel resolution s_{Vox} set in the *UfoMap* implementation, facilitating a calculation of IG at the finest level of environmental detail the map can represent. However, a challenge arises from the sheer number of endpoints and the computational demands of raycasting, especially when s_{Vox} is small. To mitigate this, a variable grid size scaling factor s_G is introduced, allowing the adjustment of endpoint density relative to s_{Vox} , effectively balancing accuracy with computational efficiency. Fig. 2a illustrates raycasting for a scaling factor $s_G = 100$ and a fixed number of perspectives $N_P = 1000$, including introduced points.

IG Calculation: To compute the IG from each perspective \mathbf{p}_P , raycasting is conducted from every \mathbf{p}_P to all related N_E endpoints \mathbf{p}_E , evaluating the voxel states along each ray. The calculation employs a straightforward metric for each perspective $j = 0, 1, \dots, N_P - 1$, based on the voxel's state and probability. This metric is designed for rapid computation, essential for real-time processing across numerous perspectives and endpoints. The IG $g_{R,k,j}$ for each

ray $k = 0, 1, \dots, N_E - 1$ of perspective j , takes states $v_i \in \{Occupied, Free, Unknown\}$ of all encountered voxels N_V on the ray into account. It reflects a cumulative assessment $g_{R,k,j} = \sum_{i=0}^{N_O} g(v_i)$ of IGs $g(v_i)$ based on whether voxels v_i are occupied, free, or unknown, as classified by the *UfoMap* based on occupancy probabilities $P(v_i)$:

$$g(v_i) = \begin{cases} 1 - P(v_i) & \text{if } v_i = \text{Occupied}, \\ P(v_i) & \text{if } v_i = \text{Free}, \\ 1 & \text{if } v_i = \text{Unknown}. \end{cases} \quad (2)$$

N_O represents the count of voxels encountered on a ray from perspective \mathbf{p}_P to the first occupied voxel or the endpoint, whichever comes first; hence, $N_O \leq N_V$. The average IG $g_{P,j}$ for a perspective j , denoted as $g_{P,j}$, is calculated by averaging the IGs from all rays emanating from that perspective, formulated as $g_{P,j} = \frac{1}{N_E} \sum_{k=0}^{N_E-1} g_{R,k,j}$.

Fig. 2b illustrates a local ID for $N_P = 1000$ perspective IGs with a grid scaling factor of $s_G = 50$. This visualization highlights that perspectives nearer to the PoI, particularly within the object's vicinity, tend to yield lower IGs because rays starting closer to the PoI encounter the object sooner.

Given its iterative nature over numerous perspectives, endpoints, and voxels for each ray, calculating this IG is highly computationally intensive. This process is suited for parallel processing on a GPU to reduce computation time significantly. A CUDA-based implementation of this algorithm facilitates the parallel evaluation of a vast number of perspectives and rays. This implementation is available in the code repository, and the performance is assessed in Section V.

IV. MOVING HORIZON PLANNING FOR NEXT-BEST-TRAJECTORIES

This section introduces the MHP for manipulators with N_{DoF} degrees of freedom and aims at computing NBTs.

General formulation of the MHP: This paragraph provides only a brief overview of the MHP. For more details, the interested reader is referred to [2], [18], [19].

The MHP, akin to Model Predictive Control (MPC), iteratively optimizes a trajectory over a finite horizon. However, unlike MPC, which often directly applies torques to the robot, this planner solely applies joint velocities to cascaded controllers. The trajectory calculation is framed as a simplified Nonlinear Programming (NLP) problem:

$$\min_{\mathbf{u}_{0:K-1}, \mathbf{x}_{1:K}} J(\mathbf{u}_{0:K-1}, \mathbf{x}_{0:K}), \quad (3a)$$

$$\text{subject to:} \quad \mathbf{x}_{k+1} = \mathbf{x}_k + \mathbf{u}_k \Delta t, \quad (3b)$$

$$\mathbf{h}(\mathbf{u}_k, \mathbf{x}_k) \leq 0, \quad (3c)$$

with $k = 0, 1, \dots, K$. Within a finite horizon K , state vectors $\mathbf{x}_k \in \mathbb{R}^{N_{DoF}}$ and control vectors $\mathbf{u}_k \in \mathbb{R}^{N_{DoF}}$ are optimized, taking into account the cost function $J(\mathbf{u}_{0:K-1}, \mathbf{x}_{0:K})$ and the inequality constraints $\mathbf{h}(\mathbf{u}_k, \mathbf{x}_k)$. The sequence of states $\mathbf{x}_{0:K}$ and controls $\mathbf{u}_{0:K-1}$ is represented by state vectors \mathbf{x}_k and control vectors \mathbf{u}_k at each step k . \mathbf{x}_k contains the robot's joint angles and \mathbf{u}_k the joint velocities. The time step Δt is the time between two steps in a discretized time grid

with $t_0 < t_1 < \dots < t_k < \dots < t_K$ with $k = 0, 1, \dots, K$. The cost function $J(\mathbf{u}_{0:K-1}, \mathbf{x}_{0:K})$ evaluates the trajectory's quality using a combination of quadratic terms for state $c_G(\mathbf{x}_k)$ and $c_C(\mathbf{u}_k)$ control vectors and an additional term $c_O(\mathbf{x}_k)$ for obstacle avoidance. For each step k , the terms are combined in $J(\mathbf{u}_k, \mathbf{x}_k) = c_G(\mathbf{x}_k) + c_C(\mathbf{u}_k) + c_O(\mathbf{x}_k)$. The inequality constraints $\mathbf{h}(\mathbf{u}_k, \mathbf{x}_k)$ encompass limits on joint angles, velocities, accelerations, and obstacle distances. A hypergraph strategy [19] enhances the optimization efficiency, and *IPOPT* [20] solves the NLP.

Cost Function Extension: The cost function $J(\mathbf{u}_{0:K-1}, \mathbf{x}_{0:K})$ is enhanced to include the IG throughout the trajectory, adding a cost term $c_I(\mathbf{x}_{0:K}) = \sum_{k=0}^K \frac{w_I}{O(\mathbf{x}_k)G(\mathbf{x}_k) + \epsilon}$. This term is defined to account for an Orientation Factor (OF) $O(\mathbf{x}_k)$ and IG $G(\mathbf{x}_k)$ at each point along the trajectory, adjusted by a weighting factor $w_I \geq 0$. For $w_I = 0$, the IG costs $c_I(\mathbf{x}_{0:K})$ vanishes. The term also includes a constant $\epsilon = 1 \times 10^{-7}$ to prevent division by zero for numerical stability. A product instead of a sum is chosen to ensure that the costs peak if either the OF or the IG is zero at state \mathbf{x}_k , reflecting that no gain is achieved if the orientation is not towards the PoI or the position does not provide any IG. The IG cost term is a barrier-like function that maximizes IG wherever possible.

OF $O(\mathbf{x}_k)$ and IG $G(\mathbf{x}_k)$: The OF $O(\mathbf{x}_k)$ quantifies how well the robot's camera is aligned with the PoI at each state \mathbf{x}_k . It compares the ideal camera orientation $\mathbf{o}_{\text{POI,I}}(\mathbf{x}_k)$, towards the PoI with the camera's actual orientation $\mathbf{o}_{\text{POI,A}}(\mathbf{x}_k)$. The OF equals the cosine of the angle between the ideal and actual camera orientation and results in $O(\mathbf{x}_k) = 1$ for perfect alignment with the target orientation and decreases for worse alignments. If the camera's orientation is outside the FoV, the OF defaults to zero, reflecting its inability to capture the PoI within its limited viewing angle. This metric ensures the robot's observations are as informative as possible by favoring poses where the camera is ideally oriented towards the PoI.

The IG $G(\mathbf{x}_k)$ assesses the amount of environmental knowledge obtained from a specific camera position associated with the robot's joint state \mathbf{x}_k . This necessitates examining the local ID, introduced in Section III, for each camera position throughout the trajectory. The local ID is limited to N_P perspectives, so not every camera position will coincide with these predefined points. To estimate the IG for any camera position, an adapted Inverse Distance Weighting (IDW) method interpolates the IGs across the nearest perspectives as

$$G(\mathbf{x}_k) = \sum_{u=0}^{N_B-1} \frac{1}{N_B - u} \frac{\sum_{j=0}^{N_P-1} g_{P,j} (d_{P,j}(\mathbf{x}_k))^{-p}}{\sum_{j=0}^{N_P-1} (d_{P,j}(\mathbf{x}_k))^{-p}}, \quad (4)$$

with the IG $g_{P,j}$ of perspective j , and the distance $d_{P,j}(\mathbf{x}_k)$ between the current camera position depending on \mathbf{x}_k and the perspective start point of perspective j . The power p serves as an adjustable parameter, allowing for the customization of the distance's impact on the interpolation process. To ensure a balance between exploration and exploitation, N_B previous IDs increase the number of perspectives N_P . The IDW result

of the previous IDs is weighted with the inverse of their position in the sequence, ensuring that older IDs have less impact than new ones.

The combination of the OF $O(\mathbf{x}_k)$ and the IG $G(\mathbf{x}_k)$ in the cost function $c_I(\mathbf{x}_{0:K})$ urges the robot's camera to be optimally oriented towards the PoI while maximizing the IG throughout the trajectory. A higher gain is achieved close to the sphere with radius r_S since these perspectives cover more unknown voxels but are still close enough to the PoI to provide valuable insights based on the choice of r_S .

Global Ergodic Trajectory: Since local planning solutions exhibit the problem of freezing robots and unknown areas due to a small horizon, a global ergodic trajectory planner [1] provides a reference trajectory to the local planner. Therefore, the repository of [1] is extended to support manipulators. The approach plans a trajectory that explores a given target distribution in an ergodic manner and decreases the overall motion time. As target distribution, the discrete ID is transferred to a continuous general mixture model using the *pomegranate library* [21]. A fixed number $N_G = 3$ of Gaussian components approximates the target distribution.

The ergodic trajectory is planned in the Euclidean space and with an inverse kinematic mapped to the robot's joint space. Note that some Euclidean points can violate the joint limits or cause self collisions, and the ergodic trajectory is then stopped at that point. The global trajectory provides intermediate waypoints for the local planner to follow, ensuring the robot explores the environment regarding the target distribution. Single waypoints of the global trajectory are not necessarily visited since the local planner may avoid them due to obstacles or high costs due to closeness to self collisions, joint limits, or low IG. Since the runtime of the global ergodic trajectory planner is significantly higher than the local planner, the global planner is executed offline once in the beginning and can replay if the user sets new start and goal points. The global ergodic trajectory planner is not further detailed in this paper, and the interested reader is referred to [1].

V. EXPERIMENTS & RESULTS

The experimental setup features a *Universal Robot UR10* with an *Azure Kinect* RGB-D camera mounted on the robot's end-effector for live data. The camera captures depth images to generate the voxel map and compute the local ID online while the robot executes the current task. The voxel resolution is set at $s_{\text{vox}} = 1$ cm. The trajectory planner operates with a $t_K = 3$ s planning horizon, a $\Delta t = 0.1$ s time step, and 10 Hz update frequency and experiments with different information weights of w_I . It employs an IDW distance power of $p = 2$ and an ID buffering with $N_B = 10$.

Online Capabilities of the Information Distribution

A CUDA-based implementation allows for parallel processing of IGs for perspectives on a GPU, improving efficiency and providing the planner with faster updated IG maps. This experiment examines the impact of the number of perspectives N_P and the scaling factor s_G on GPU runtimes, comparing these against a sequential Central Processing Unit (CPU)

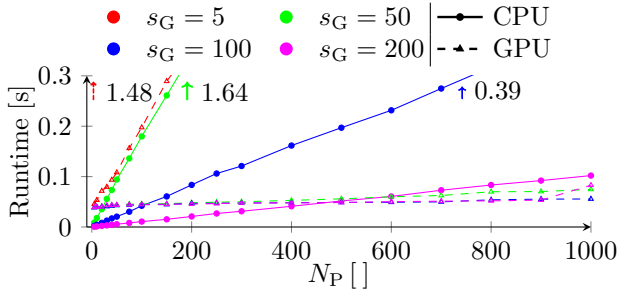


Fig. 3: Mean runtimes of GPU and CPU over 100 iterations for the ID with various s_G and N_P .

implementation. The comparison is conducted by replaying a recorded *Azure Kinect* stream and measuring the runtime of ID calculations on both the CPU and GPU. The hardware comprises an *Intel Core i5-12600KF* CPU, *NVIDIA GeForce RTX 3060* GPU, and 32 GB RAM.

The data in Fig. 3 illustrates the mean runtimes across 100 iterations for the GPU (dashed lines) and CPU (solid lines) versions of the local ID calculation. The comparison covers a range of grid scaling factors s_G and varying numbers of perspectives N_P . To enhance clarity and emphasize the comparison, the y -axis in the graph is capped at 0.3s. Note that due to the capping of the y -axis, the CPU runtime with $s_G = 5$ is not visible in the graph but reaches a final runtime of 144.93 s for $N_P = 1000$. Other specific runtimes are noted directly in the figure for configurations with longer runtime. The GPU implementation outperforms the CPU across all configurations tested. Specifically, for $N_P = 1000$, the GPU’s average runtime decreases by approximately 75% across various scaling factors s_G compared to the CPU implementation, showcasing significant efficiency improvements.

The efficiency benefits of using the GPU for computations become more significant as the number of rays increases since the GPU implementation involves extra memory allocation and data transfer, which can be time-consuming when dealing with a low number of rays. This effect is clearly illustrated in Fig. 3, where the GPU exhibits longer runtimes for smaller numbers of perspectives N_P . The runtime advantage gets more significant with more perspectives, for example, visible for $s_G = 200$, where the GPU runtime is higher than the CPU runtime up to approximately $N_P = 500$.

This study opts for $s_G = 100$ and $N_P = 500$ to maintain swift IG calculations for real-time planning.

Next-Best-Trajectory

This section assesses the influence of the information cost term c_1 on the NBT of the robot manipulator, as well as the integration of a global ergodic reference trajectory. It is divided into four experiments, each exploring different aspects. A supplementary video of the experiments is provided. The first experiment assesses the influence of the information cost term c_1 on trajectory planning in general, while the second experiment investigates the difference compared to a baseline that applies an NBV strategy. The third experiment evaluates the influence of a human working in the environment, and

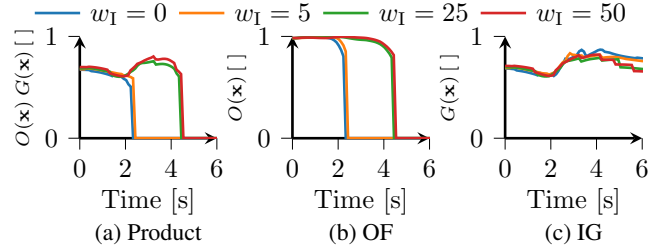


Fig. 4: Product (a) of OF (b) and IG (c) along the NBT with different weights w_I until \mathbf{x}_{goal} is reached.

the fourth experiment investigates the influence of a global ergodic reference trajectory on the robot’s behavior.

The evaluation metrics include the achieved product of IG and OF and its Area Under the Curve (AUC). Additionally, the remaining IG, which reflects unseen information due to unknown voxels or revisiting previously observed voxels, is analyzed. The reconstruction of an object at the PoI over time is also examined by evaluating the percentage volumetric change V_R , compared to a voxel map of the object from a stationary perspective without demonstrator occlusion. Therefore, $V_R = 0\%$ indicates a reconstruction of the reference map without additional voxels, while $V_R > 0\%$ signifies a reconstruction with more voxels, and $V_R < 0\%$ indicates a reconstruction with fewer voxels than the reference map. It is important to note that this basic metric does not account for duplicate voxels caused by mapping inconsistencies or rapid movements and only provides an initial indication of the reconstruction potential and speed. This section only conducts experiments considering both IG and OF terms within the costs since the combination of position and orientation is required to generate valuable views of the PoI.

Experiment I: Experiment I evaluates the impact of the information cost term c_1 on the robot’s trajectory planning with different weights w_I . The robot task is a motion from $\mathbf{x}_{start} = [-1.57 \ 0 \ 0 \ 0 \ 1 \ 0]^T$ to $\mathbf{x}_{goal} = [1.57 \ -0.75 \ 0 \ 0 \ 0 \ 0]^T$. While the start position is oriented towards the PoI inside the demonstrator (see red dots Fig. 1), the goal position is not facing the PoI to check the robot’s capability to keep its orientation towards the PoI during the motion. Fig. 1 shows the results of the robot 3.5 s after starting the task with different information weights $w_I = 0$, $w_I = 5$, $w_I = 25$, and $w_I = 50$ (left to right). It is visible that the orientation towards the PoI benefits from increasing w_I .

Fig. 4 shows that increasing w_I leads to a better orientation (b) towards the PoI and, therefore, in an increased $O(\mathbf{x})G(\mathbf{x})$ (a), signifying a better data collection of the object. Note that the time axis is capped at 6 s to increase the readability of the plot for lower times. The AUC of $O(\mathbf{x})G(\mathbf{x})$ over the trajectory is 1.34 ± 0.03 for $w_I = 0$, 1.53 for $w_I = 5$, 2.89 ± 0.05 for $w_I = 25$, and 3.13 for $w_I = 50$. Note that the results of $w_I = 0$ and $w_I = 25$ are mean values and standard deviations of five trials to show that the approach is repeatable, generating similar results. The total travel time increases with higher w_I due to the robot’s focus on areas

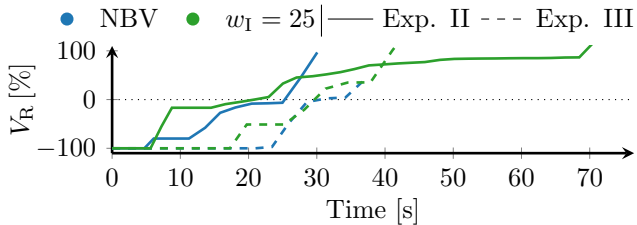


Fig. 5: V_R over time for experiment II (solid) and III (dashed).

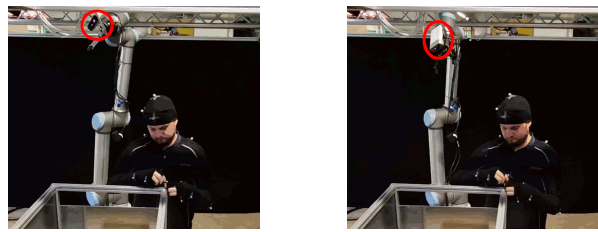
with higher informational value, leading to an increase from 7s without optimizing the IG to 13.1s for $w_I = 50$. For $w_I = 0$ and $w_I = 5$, no reconstruction of the object inside the demonstrator is possible. The robot can reconstruct the object for $w_I = 25$, and $w_I = 50$, and V_R is 14.72% and 42.78%, respectively. This indicates that both weights lead to a reconstruction with more voxels than the reference map due to the robot’s motion. As a compromise of the results between runtime and reconstruction, $w_I = 25$ is chosen for the following experiments.

Experiment II: Experiment II compares the results of the NBT with a baseline that applies an NBV strategy [12]. The robot starts at $\mathbf{x}_{\text{start}}$, and based on the ID, the first NBV is selected and used for the following goal configuration. This is repeated for the five subsequent NBVs overall. These poses serve as goals for the baseline, and the robot moves towards these without considering the optimization, $w_I = 0$, but still using the MHP, and once with the MHP and $w_I = 25$.

The AUC of the baseline is 17.23, and the AUC of the NBT approach is 40.26, but the total execution time increases from 30.50s to 75.13s since the optimization of the IG leads to robot motions that leave areas with higher gain slower. Due to the usage of NBV poses as goals, the reconstruction of the object is possible for both trials. However, the remaining IG and the reconstruction time differ for the experiment. The remaining IG is calculated by averaging the last $N_B = 10$ IG PCs. For the baseline approach, the remaining IG is 0.60; for the NBT approach, the remaining IG is 0.47, signifying a reduction of 21.67%. The solid lines in Fig. 5 show the reconstruction over time for both. It is visible that the same volume as in the reference map $V_R = 0\%$ is reached approximately 4s later for the NBV compared to the NBT approach. Nevertheless, both approaches reconstruct the model with more voxels than the reference due to the robot motion and camera and map mismatches over time.

Experiment III: Experiment III assesses the impact of human activity within the environment on the robot’s trajectory planning. The setup is identical to that in Experiment II, but with a human moving screws from the robot’s side of the demonstrator to the opposite side, intermittently interfering with the robot’s motion. To accommodate the added computational load, the planning horizon is shortened to $t_K = 2$ s. The MHP treats the human as an obstacle and adjusts the trajectory accordingly while attempting to achieve the sequence of goals. Note that human movements may vary between trials, leading to different outcomes for the robot, but the concept of the approach is demonstrated.

Fig. 6 directly compares NBV and NBT approaches with a



(a) NBV

(b) NBT

Fig. 6: Working human during the robot’s motion for the NBV (a) and NBT (b) approach.

human working in the environment. It is evident that the NBT approach results in better orientation towards the PoI within the demonstrator, whereas the NBV approach prioritizes quicker access to the first goal pose at the expense of less optimal orientation during the motion.

The dashed lines in Fig. 5 show the reconstruction over time for NBV and NBT and that the human influences the reconstruction such that it starts later since the human blocks the way towards the first goal pose. However, the NBT reaches $V_R = 0\%$, approximately 1s earlier than the NBV approach.

Experiment IV: Experiment IV evaluates the influence of a global ergodic reference trajectory on the robot’s behavior. Therefore, the robot starts at $\mathbf{x}_{\text{start}}$ and aims to reach $\mathbf{x}_{\text{goal}} = [1.57 \ 0 \ 0 \ 0 \ 0]^T$. The global ergodic reference trajectory guides the robot to the goal configuration and enables an ergodic exploration regarding the target distribution.

When relying solely on the MHP, the robot halts before the demonstrator and fails to reach the goal. In contrast, when using the ergodic reference in combination with the MHP with $w_I = 0$ and $w_I = 25$, the robot successfully reaches the goal pose, resulting in an increase in IG. Similar to previous results, applying $w_I = 25$ leads to an improved view of the PoI inside the demonstrator, increasing the AUC by 28.85%, decreasing the remaining IG by 12.43% and reaching $V_R = 0\%$ approximately 2s earlier.

VI. CONCLUSION & OUTLOOK

This paper presents a novel approach to improve observation and reconstruction in robotics by maximizing IGs along the robot’s trajectory. Leveraging GPU-based IG estimation from perspectives around a PoI, the method enables real-time ID analysis. The local trajectory planner integrates this data to determine the NBT, optimizing for IG while ensuring collision avoidance, especially in human-robot interactions. A global ergodic planner provides a reference trajectory, enhancing exploration and preventing standstills.

Future research will refine parameter configurations for the global ergodic planner to enhance exploration and adapt ID to different PoI shapes. Additionally, integrating various IG metrics into the MHP will optimize cost functions and weighting strategies. Real-world experiments will examine the capability, quality and efficiency of automated data collection for training machine learning models in robotics. An open-source OpenCL implementation of parallelized gain

metric computation will be explored to benefit the broader community.

REFERENCES

- [1] D. Dong, H. Berger, and I. Abraham, "Time optimal ergodic search," in *Robotics: Science and Systems XIX*. Robotics: Science and Systems Foundation, 2023.
- [2] H. Renz, M. Krämer, and T. Bertram, "Moving horizon planning for human-robot interaction," in *ACM/IEEE International Conference on Human-Robot Interaction (HRI)*, 2024.
- [3] N. Dengler, S. Pan, V. Kalagaturu, R. Menon, M. Dawood, and M. Bennis, "Viewpoint push planning for mapping of unknown confined spaces," in *IEEE/RSJ International Conference on Intelligent Robots and Systems (IROS)*, 2023.
- [4] A. Hornung, K. M. Wurm, M. Bennis, C. Stachniss, and W. Burgard, "OctoMap: an efficient probabilistic 3D mapping framework based on octrees," *Autonomous Robots*, vol. 34, no. 3, 2013.
- [5] H. Min, K. M. Han, and Y. J. Kim, "OctoMap-RT: Fast probabilistic volumetric mapping using ray-tracing GPUs," *IEEE Robotics and Automation Letters*, vol. 8, no. 9, 2023.
- [6] D. Duberg and P. Jensfelt, "UFOMap: An efficient probabilistic 3D mapping framework that embraces the unknown," *IEEE Robotics and Automation Letters*, vol. 5, no. 4, 2020.
- [7] R. Monica and J. Aleotti, "Contour-based next-best view planning from point cloud segmentation of unknown objects," *Autonomous Robots*, vol. 42, no. 2, 2018.
- [8] T. Overbye and S. Saripalli, "G-VOM: A GPU accelerated voxel off-road mapping system," in *IEEE Intelligent Vehicles Symposium (IV)*, 2022.
- [9] M. Grinvald, F. Furrer, T. Novkovic, J. J. Chung, C. Cadena, R. Siegwart, and J. Nieto, "Volumetric instance-aware semantic mapping and 3D object discovery," *IEEE Robotics and Automation Letters*, vol. 4, no. 3, 2019.
- [10] A. Bircher, M. Kamel, K. Alexis, H. Oleynikova, and R. Siegwart, "Receding horizon "next-best-view" planner for 3D exploration," in *IEEE International Conference on Robotics and Automation (ICRA)*, 2016.
- [11] L. Lu, C. Redondo, and P. Campoy, "Optimal frontier-based autonomous exploration in unconstructed environment using RGB-D sensor," *Sensors*, vol. 20, no. 22, 2020.
- [12] J. Santos, M. Oliveira, R. Arrais, and G. Veiga, "Autonomous scene exploration for robotics: A conditional random view-sampling and evaluation using a voxel-sorting mechanism for efficient ray casting," *Sensors*, vol. 20, no. 15, 2020.
- [13] J. Delmerico, S. Isler, R. Sabzevari, and D. Scaramuzza, "A comparison of volumetric information gain metrics for active 3D object reconstruction," *Autonomous Robots*, vol. 42, no. 2, 2018.
- [14] S. Pan and H. Wei, "A global generalized maximum coverage-based solution to the non-model-based view planning problem for object reconstruction," *Computer Vision and Image Understanding*, vol. 226, 2023.
- [15] B. Lindqvist, A. Patel, K. Löfgren, and G. Nikolakopoulos, "A tree-based next-best-trajectory method for 3-d uav exploration," *IEEE Transactions on Robotics*, vol. 40, 2024.
- [16] R. B. Rusu and S. Cousins, "3D is here: Point cloud library (PCL)," in *IEEE International Conference on Robotics and Automation (ICRA)*, 2011.
- [17] M. E. Muller, "A note on a method for generating points uniformly on n-dimensional spheres," *Communications of the ACM*, vol. 2, no. 4, 1959.
- [18] M. Krämer, C. Rösmann, F. Hoffmann, and T. Bertram, "Model predictive control of a collaborative manipulator considering dynamic obstacles," *Optimal Control Applications and Methods*, vol. 41, no. 4, 2020.
- [19] C. Rösmann, M. Krämer, A. Makarow, F. Hoffmann, and T. Bertram, "Exploiting sparse structures in nonlinear model predictive control with hypergraphs," in *IEEE/ASME International Conference on Advanced Intelligent Mechatronics (AIM)*, 2018.
- [20] A. Wächter and L. T. Biegler, "On the implementation of an interior-point filter line-search algorithm for large-scale nonlinear programming," *Mathematical Programming*, vol. 106, no. 1, 2006.
- [21] J. Schreiber, "Pomegranate: fast and flexible probabilistic modeling in python," *Journal of Machine Learning Research*, vol. 18, no. 164, pp. 1–6, 2018.